Preliminary Results from a Prototype Ocean-Bottom Pressure Sensor Deployed in the Mentawai Channel, Central Sumatra, Indonesia

LEE FREITAG[1] and EMILE A. OKAL[2]

Abstract—We analyze data retrieved from an ocean floor pressure sensor continuously operated for 48 days in the Mentawai Strait during the Spring of 2016, as part of Project Hazard SEES. Initial processing through systematic spectrogram analysis has identified ten distant earthquakes recorded through the variation of pressure accompanying the passage of seismic waves on the bottom of the ocean. The analysis of the corresponding wavetrains allows the recovery of the standard magnitude M_s of seven of the events (two more being intermediate depth, and the tenth antipodal) with a residual not exceeding 0.3 logarithmic units. We also show that the classical energy-to-moment ratio computation can be successfully adapted by defining a response function of the pressure sensor to teleseismic P waves. In addition, six local earthquakes, occurring at distances of 58–670 km from the sensor, but with moment magnitudes less than 5.7, were also recorded. We show that an estimate of the seismic energy radiated by these events can be obtained from a simple integration of the square of the pressure signal. Thus our results indicate that meaningful quantitative estimates of the source characteristics of both teleseismic and regional events can be obtained through robust methods based on single-station pressure recordings on the ocean floor.

Keywords: Tsunamis, ocean bottom sensors, seismic waves.

1. Background and Motivation

The purpose of this paper is to report on the prototype operation of a precision ocean bottom pressure sensor, in order to estimate the magnitudes of both nearby and distant teleseismic events in the context of tsunami warning in the Mentawai Strait, bounded to the Southwest by the island of Siberut, and to the Northeast by the large island of Sumatra

(Fig. 1). The sensor was installed in the Spring of 2016 for slightly less than 2 months as an initial test in this active seismic area, within the Mentawai Basin, a body of water approximately 1800 m deep separating the main island of Sumatra from a string of forearc islands

The relevant section of the Sumatra subduction zone is believed to have ruptured in the mega earthquakes of 1797 (northern half) and 1833 (southern part), and to have been locked ever since (Zachariasen et al. 1999; Natawidjaja et al. 2006), contrary to the next segment to the South, where at least part of the tectonic convergence accumulated since 1833 was released during the 2007 Bengkulu earthquake (Borrero et al. 2009). This region is therefore interpreted as a seismic gap, where conditions are ripe for a megathrust event to take place in the next years or decades, which would generate a tsunami with potentially catastrophic consequences for the nearby port city of Padang (2019 metropolitan population: 1.4 million) (Borrero et al. 2006).

The pressure sensor is intended for use in a tsunami detection system that is conceptually similar to that of the DART buoys (Meining et al. 2005). However, instead of transmitting detections via acoustic modem to a nearby surface buoy, the system will transmit to a seafloor station that is cabled to shore, and do so at ranges of 20–30 km over a mostly horizontal path. In this context, the proposed acoustically-linked system is a prototype of a method for near-field warning that may find use under specific circumstances where a cabled sensor is impossible or impractical. In particular, it eliminates the need for a surface buoy, which requires maintenance and is subject to damage from ocean forces or vandalism (Mungov et al. 2013). Cabled pressure sensors

[1] Woods Hole Oceanographic Institution, MS 18, Woods Hole, MA 02543, USA.
[2] Department of Earth and Planetary Sciences, Northwestern University, Evanston, IL 60208, USA. E-mail: emile@earth.northwestern.edu
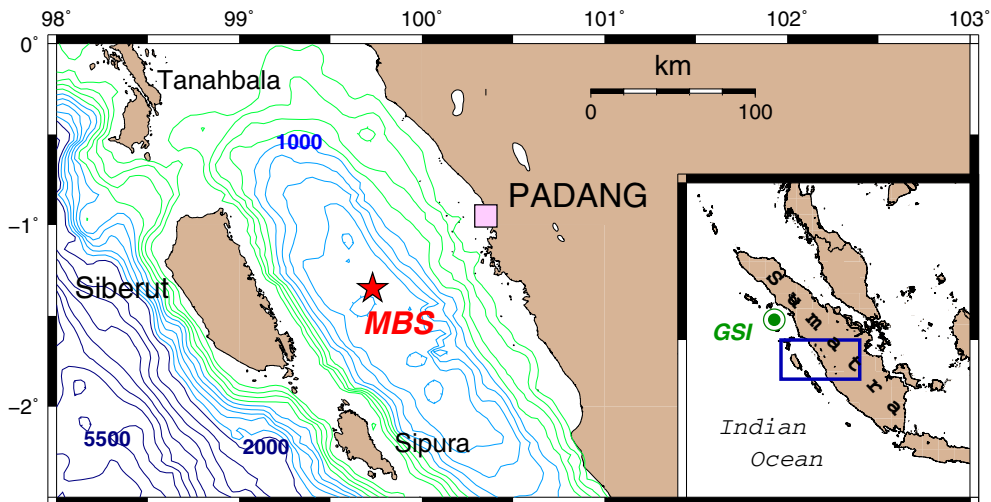
Figure 1
Location of instrument deployment at MBS (red star), in the Mentawai Channel, about half-way between the city of Padang and the Island of Siberut. Isobaths are at 200 m interval (200–800 m in green; 1000–1800 m in light blue), and at 500-m interval at depths of 2000 m and greater (dark blue). The location of the main map is shown as the box on the reference map at right; the bull's eye symbol identifies the GEOFON station GSI on Nias Island

combined with broadband seismometers will always remain a preferred method for tsunami warning in the near field, but it is hoped that our approach will provide governmental authorities with additional options.

In addition, the time sampling used in our experiment ($\delta t \approx 0.05$ s) allows a full broadband seismic processing of the time series, in contrast to the coarse sampling used by DART buoys. The seafloor sensor will still require regular maintenance including battery changes, so minimizing its energy budget is critical. This motivates the use of a single pressure sensor as opposed to a complete broadband motion package such as those employed in standard three-component ocean-bottom seismometers. Therefore it is desirable to extract as much useful information as possible from the pressure sensor, including the magnitude of P and Rayleigh waves impinging on the ocean bottom unit. The work presented here reviews the results of an initial approach toward that use.

2. Operational Aspects

The instrument deployed consists of a Paroscientific (USA) Digiquartz® nano-resolution pressure

sensor Model 8CB2000-I, which includes pre-processing of the native frequency output, available as an ASCII serial data stream (Paros et al. 2012). The instrument was deployed on a platform which rests on the seafloor and is equipped with a pressure sensor, data logger, battery and acoustic release for recovery. The platform, termed a lander because it rests directly on the sea floor, is deployed from a surface vessel and it free-falls to the bottom (Fig. 2).

The instrument was deployed in the vicinity of 1.350° S, 99.733° E (hereafter Mentawai Basin Site or MBS), at a depth $H \approx 1750$ m (Fig. 1). The above coordinates refer to the sea-surface location where the instrument was dropped, which is estimated to coincide with its resting position within uncertainties on the order of a few hundred meters. The exact depth of deployment was provided by the sensor itself (see below). Recording was performed at a sampling rate of 22 samples per second, and the raw data stored as pressure time series expressed in pounds[-force] per square inch (psi), later converted to metric units through the factor

$$1 \text{ psi } = 68972 \text{ dyn/cm}^2 = 6897.2 \text{ Pa} \quad (1)$$

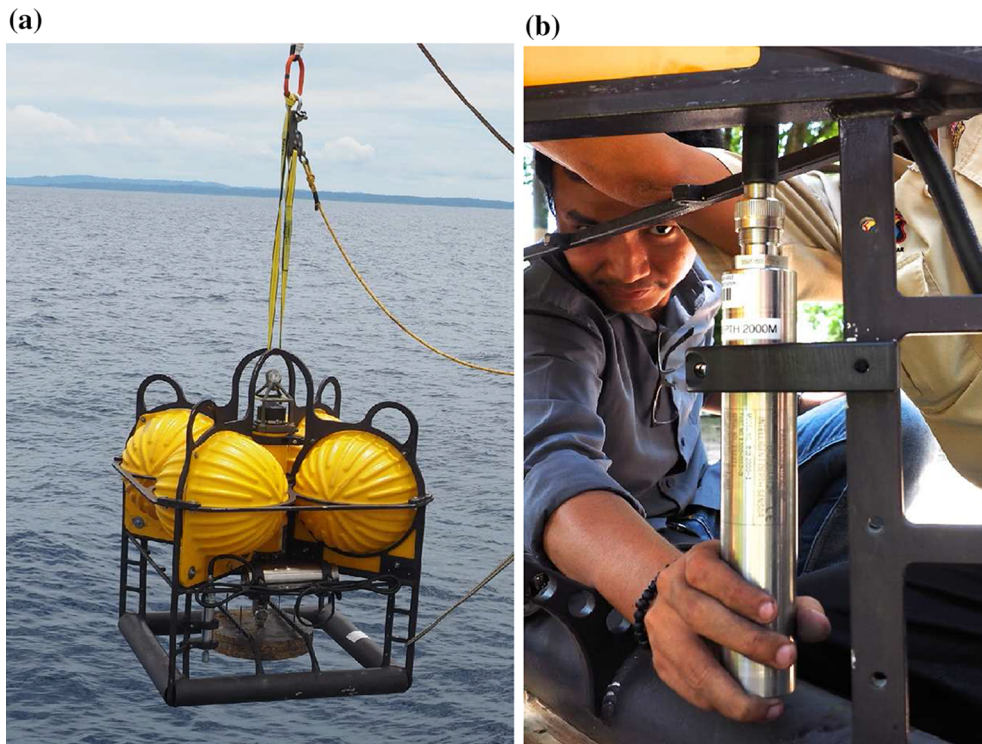The instrument was deployed on 23 March 2016 (Fig. 2), and retrieved on 12 May 2016. It provided a

(a)   **(b)**

Figure 2
a Deployment at sea of instrument at Location MBS, 23 March 2016. **b** Close-up of instrument showing pressure sensor

continuous stream of data from 26 March to 12 May 2016, or 48 days.

Figure 3 is an example of a 24-h time series obtained for 13 April 2016, containing the record of an intermediate-depth earthquake in Myanmar ($M_0 = 3.2 \times 10^{26}$ dyn $*$ cm ($M_w = 6.9$); $h = 136$ km; hereafter Event T6). It is easily verified that the average value recorded (~ 2550 psi) is the hydrostatic pressure of the water column at the site, $p = \rho_w g H$, which translates into a depth $H = 1744$ m, using a density $\rho_w = 1.03$ g/cm^3 and $g = 979$ cm/s^2, appropriate near the Equator. Additionally, the peak-to-peak amplitude of the tidal signal, typically 1.15 psi, translates into an amplitude of 79 cm for the oceanic tide, which compares favorably with tides typically on the order of 1.2 m peak-to-peak in the port of Padang, given the expected influence of the response of the harbor. These observations provide an independent check of the proper calibration of the instrument.

3. Data Processing

Figure 4 presents the spectrum of a one-day long window of data, recorded in the absence of detectable seismic signals, on 09 April 2016. For reference, we compare it to the spectrum of the vertical broadband channel at the seismic station GSI, operated by GEOFON at Gunungsitoli, on nearby Nias Island, the distance between the two sites being 380 km (Fig. 1). These spectra have not been corrected for instrument response, since in the case of the pressure sensor and as discussed below, the conversion to ground motion involves different functions depending on the nature of the seismic wave recorded; rather, the figure is simply intended to explore the level of background noise, and hence the feasibility of extracting seismic signals in various frequency bands. The vertical scales are common logarithmic units, but unrelated in an absolute sense,
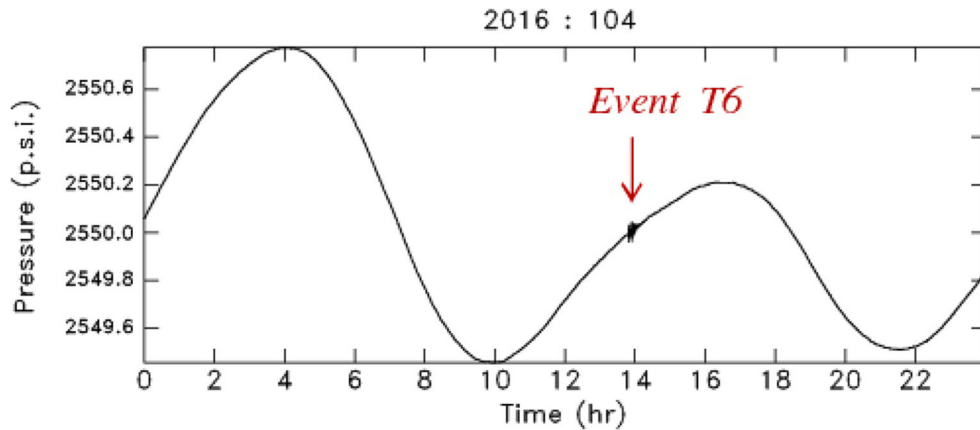
Figure 3
Example of raw 24-h time series recorded at MBS on 13 April 2016. The main oscillation expresses the tide. The signal around 14:00 GMT is Event T6, an intermediate depth earthquake in Myanmar

thus allowing a *relative* comparison of the levels of background noise as a function of frequency. Between 1 and 10 s (0.1 and 1 Hz), the land site is dominated by microseismic noise due to the harmonics of sea swell, an ubiquitous feature of coastal seismic stations; by contrast, and expectedly, these are absent from the seafloor record, as is the fundamental of the swell, around 12 s. While the noise at the seafloor site is relatively low beyond 30 mHz ($T < 30\,\mathrm{s}$), it increases substantially at lower frequencies, in sharp contrast to the seismic spectrum at GSI. Unfortunately, this will prevent a quantitative interpretation of surface waves at periods $T \geq 30\,\mathrm{s}$. The origin of this effect is presently unknown.

All 48 available 24-h time windows of data were then submitted to a classical spectrogram analysis, consisting of Fourier-transforming a running window and plotting the resulting spectral amplitude as a function of time and frequency (Cohen 1989). This procedure allows the systematic detection of events recorded by the instrument, even when their signal is not directly apparent in the time series, as exemplified by Event T5 on Fig. 5.

4. Processing of Teleseismic Events

Ten teleseismic earthquakes, listed in Table 1 and mapped on Fig. 6, were detected in the present experiment. Their seismic moments range from 1.1×10^{25} dyn $*$ cm for event T7, a small earthquake in Mindanao, to 5.9×10^{27} dyn $*$ cm, for Event T9, the large 2016 Muisne, Ecuador earthquake with its epicenter essentially antipodal to MBS ($\Delta = 178.95°$).

4.1. Rayleigh Waves

In order to examine the long-period properties of our records, we first focus on Rayleigh waves. Elementary seismic theory (e.g., Haskell 1953) shows that a pressure sensor at the interface between a solid half-space and an ocean of thickness H records a Rayleigh wave as an overpressure of amplitude

$$P = \rho_w \, \omega^2 H \cdot u_z \qquad (2)$$

where u_z is the vertical seismic displacement of the solid Earth. In other words, the pressure sensor functions as an accelerometer whose gain is proportional to the depth of the water column. At a depth of 1750 m, the vertical displacement of the Rayleigh wave can be restored by first converting the digital values (pounds-force per square inch) to metric units using Eq. (1), and then representing the sensor as an instrument featuring two null "zeroes" and no poles, with a total magnification of $-\rho_w H = -1,802,000\,\mathrm{kg/m^2}$.

Because of the excessive noise in the frequency band of mantle waves, it was not possible to compute
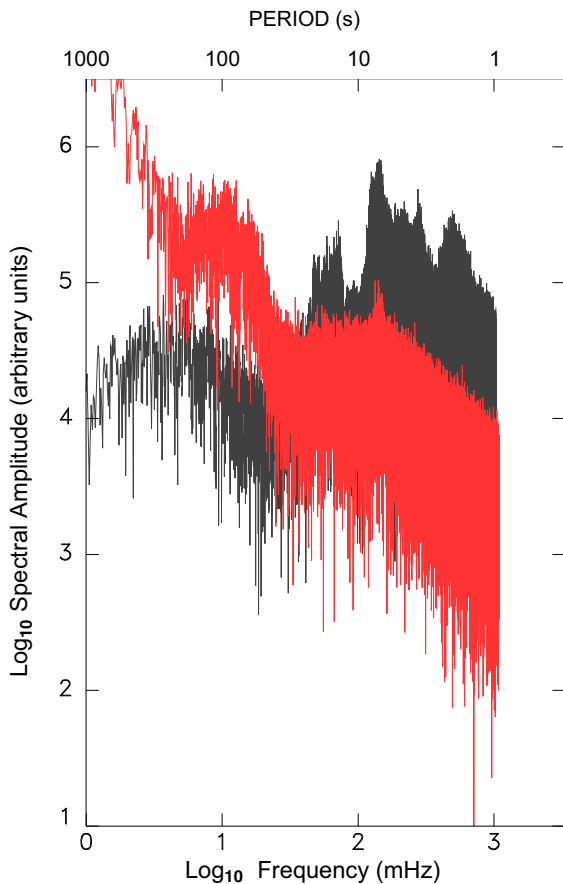
Figure 4

Spectral amplitude (in red) of 24-h record at MBS in the absence of seismic signal (09 April 2016). For reference, the corresponding spectrum at the nearby GEOFON station GSI is given in black. The vertical scales for logarithmic units are common to both plots, but their baselines are different, allowing for direct comparison of the repartition of background noise across the frequency spectrum. Note strong noise at MBS for $T \geq 30$ s

mantle magnitudes (Okal and Talandier 1989) which would have allowed the retrieval of a long-period seismic moment. Rather, we had to limit our investigations to conventional surface-wave magnitudes, using the Prague formula (Vaněk et al. 1962)

$$M_s \ = \ \log_{10} \left[\frac{A}{T} \right] \ + \ 1.66 \log_{10} \Delta \ + \ 3.3 \quad (3)$$

where A is in microns, T in seconds, and Δ in degrees. For each record, we extract a 1-h time window containing the Rayleigh wavetrain, and filter it between 10 and 30 s. A time-domain measurement of the maximum amplitude can be converted into a

displacement using (2), which substituted into (3) leads to

$$M_s \ = \ \log_{10} \left(p \cdot T \right) \ + \ 1.66 \log_{10} \Delta \ + \ 5.3 \quad (4)$$

where p is in psi. As detailed on Table 1, we obtain M_s values in excellent agreement with published ones; note that we do not compute M_s for Events T5 and T6 which are at intermediate depths, nor for T9, where the station is antipodal ($\Delta \ = \ 179°$).

We conclude that the pressure sensor can be used reliably to quantify the amplitude of conventional 20-s Rayleigh waves from teleseismic events in the range $M_s = 5.4$–7.2. Unfortunately, the only significantly larger event recorded during our deployment was antipodal, and also, the presence of unexplained but significant noise at longer periods prevented the extension of our investigations to the domain of mantle waves more directly associated with tsunami excitation.

4.2. P waves

We use P waves recorded by the pressure sensor from teleseismic events to compute an energy flux at the receiver, and from there an estimate of the seismic energy radiated by the source, following the algorithm of Newman and Okal (1998), itself inspired by Boatwright and Choy (1986).

At the bottom of a liquid layer where the sound velocity is α_w, it can be shown that, upon incidence of a P wave, the impedance ratio of pressure in the fluid to vertical displacement at the interface is

$$Z \ = \ \frac{P}{u_z} \ = \ \rho_w \, \alpha_w \, \omega \quad (5)$$

meaning that a pressure sensor will now respond to ground velocity, which amounts to adding a factor $(\alpha_w \, / \, \omega H)$ to the response used for surface waves.

An additional complexity stems from multiple reflections in the water column. This effect can be considered the conjugate, at the receiver, of the well known source-side generation of multiply reflected $pmwP$ phases (Mendiguren 1971). The classical surface response coefficient for incident P waves, $C^P(i_0)$ in the notation of Okal (1992), which adds the contribution to ground motion of reflected P and SV waves at the surface, must be replaced by a water
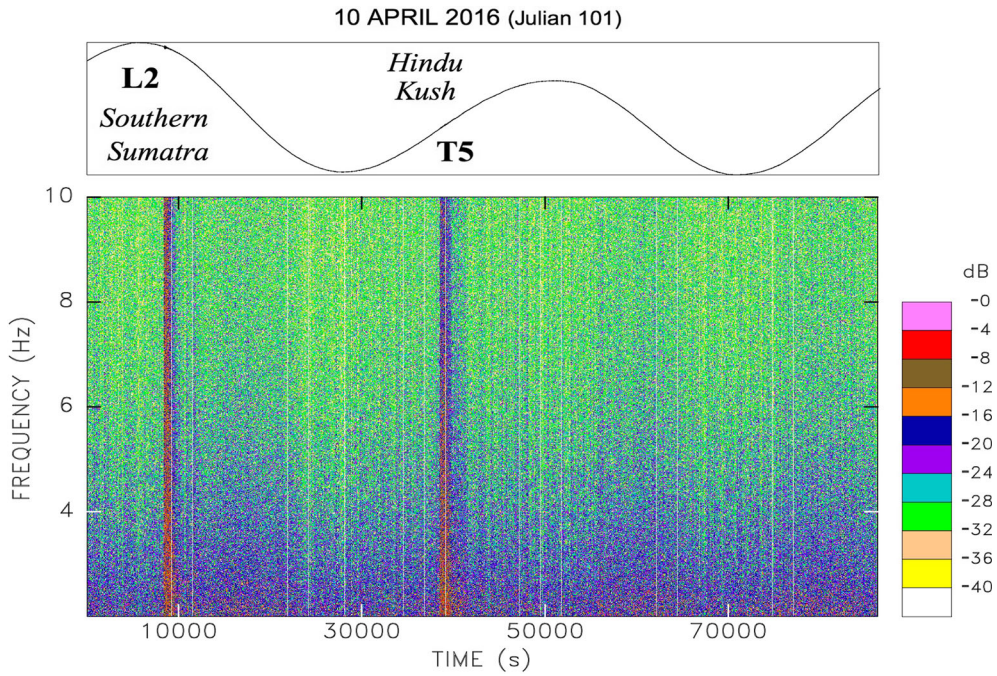
Figure 5
Spectrogram of a 1-day window of data. Spectral amplitudes are computed between 2 and 10 Hz using a 100-s long moving window offset in 50-s slices, and color-coded according to the palette at right. This procedure clearly detects both the regional event L2 in Southern Sumatra, and the teleseismic intermediate-depth earthquake T6, the latter appearing only as traces in the raw barogram (Top)
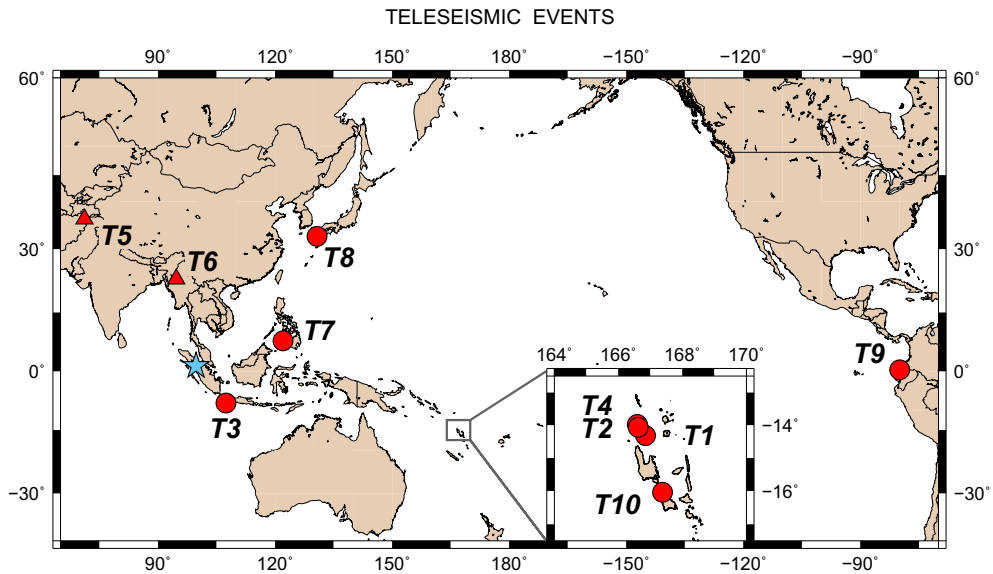

Figure 6
Map of the epicenters of earthquakes detected at teleseismic distances by the pressure sensor at MBS (blue star). The inset zooms on the grey box on the main map, to detail the four Vanuatu events. Shallow events ($h < 70$ km) are shown as full circles, intermediate ones as triangles. Codes refer to Table 1
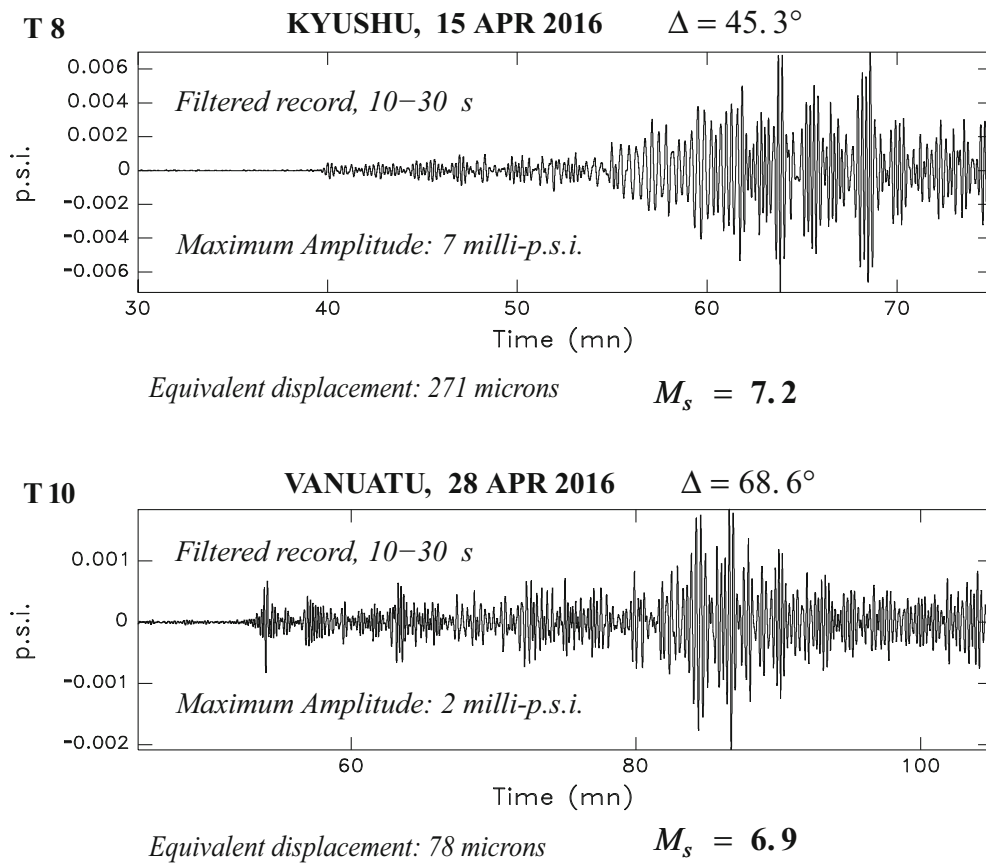
Figure 7
Examples of computation of surface-wave magnitude M_s at MBS for teleseismic events T8 (Kyushu) and T10 (Vanuatu). See text for details

layer response. At the high frequencies characteristic of P waves, it is appropriate to sum the energies of the various rays involved in the multiple reflections (Fig. 8), which conceptually add up to

$$RESP^2 \;=\; 2\, T_{SL}^2 \sum_{j=0}^{\infty} \left(R_{LL}^2\right)^j \;=\; 2\, \frac{T_{SL}^2}{1\,-\,R_{LL}^2} \quad (6)$$

where $T_{SL} = T$ and $R_{LL} = R$ are amplitude coefficients for solid-liquid transmission and liquid–liquid reflection at the solid-liquid interface, respectively. The coefficient $RESP$ then replaces $C^P(i_0)$ in Okal's (1992) formalism. A special algorithm is used for Events T5 and T6, whose depths are intermediate (Saloor and Okal 2018), and an additional correction effected for Events T3, T6 and T7, for which the station is less than $30°$ away (Ebeling and Okal 2012).

Table 1 includes values of estimated energies E^E for nine teleseismic events (the computation is not carried out for the antipodal event T9), as well as parameters $\Theta = \log_{10}(E^E / M_0)$, obtained using published values of the seismic moments M_0 of the relevant earthquakes. These are compared to values of Θ computed routinely from a global dataset of stations (Newman and Okal 1998; Saloor and Okal 2018). As shown on Fig. 9, the agreement is excellent, with no systematic trend in the residual between the pressure sensor Θ and its reference value; as for the root-mean-square of the residual (0.21 logarithmic units), it is comparable to the scatter of individual station values, when using large global datasets at seismological stations.

Attempts to include teleseismic events with lower moments proved unsuccessful. In particular, the
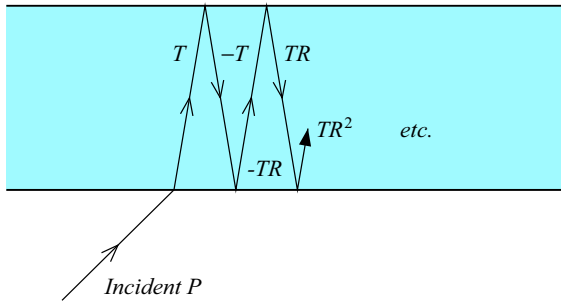
Figure 8
Multiple reflections and response function of the oceanic column for a teleseismic P wave recorded as a pressure signal at the bottom of the ocean. See text for details

Figure 9
Comparison of values of the slowness parameters Θ obtained from a global dataset (abscissa) and from the pressure sensor at MBS (ordinate)

earthquakes on 16 April 2016 in Kyushu (O.T. 12:26 and 15:03 GMT; $M_0 = 2.3$ and 1.2×10^{25} dyn*cm ($M_w = 6.2$ and 6.0), respectively), and the Vanuatu event on the same day (O.T. 21:50; $M_0 = 3.3 \times 10^{25}$ dyn $* $ cm ($M_w = 6.3$)) had P waves not meaningfully detected above noise level, by contrast with the comparatively-sized Events T3 in Java and T7 in Mindanao. As expected, these results emphasize the crucial effect of distance on the moment threshold for computation of radiated energy from our pressure sensor time series.

5. Processing of Local Events

Six regional earthquakes, listed in Table 2 and mapped on Fig. 10, were detected in the present experiment. Two of those (L1 and L5) took place at intermediate depths in the downgoing slab under Sumatra. Except for the small Event L6, also closest to the pressure sensor at only 58 km, all had a moment tensor inverted as part of the GlobalCMT project (Dziewonski et al. 1981; Ekström et al. 2012), with moments listed in Table 2, and best-fitting double-couples shown on Fig. 10; note the diversity in focal geometries, which illustrates the oblique convergence at the Sumatra trench (Sella et al. 2002).

At regional distances, an empirical estimate of earthquake size can be obtained by simply integrating the energy flux of the time series of overpressure. By analogy with energy estimates computed at
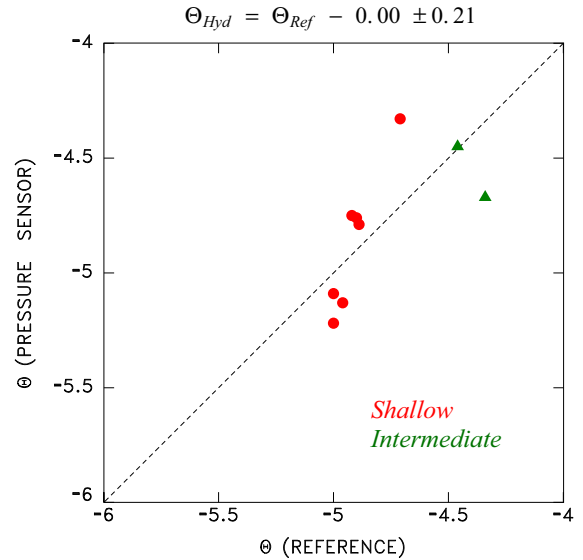
teleseismic distances (Boatwright and Choy 1986; Newman and Okal 1998), we simply consider the pressure flux

$$F^P = \frac{\alpha_w}{\pi} \int \frac{|P|^2(\omega)}{K} \cdot d\omega \qquad (7)$$

where $P(\omega)$ is the Fourier transform of the pressure $p(t)$, and α_w and K, the sound velocity and bulk modulus of the water, respectively; by analogy with computations of estimated energy, the integral in (7) is conveniently limited to the window 0.1–2 Hz. Note that we neglect anelastic attenuation at regional distances. Through a further, and admittedly drastic simplification, an estimate of the total energy of the seismic source is then obtained by scaling F to the square of the epicentral distance D and weighting the result to include the contribution of S waves, to obtain a pressure-estimated energy

$$E_P^E = 4\pi \cdot D^2 \cdot (1 + q^{BC}) \cdot F^P \qquad (8)$$

where q^{BC} is given by Newman and Okal (1998) after Boatwright and Choy (1986). For Event L6, at a distance smaller than 100 km, the far-field approximation to the body wavefield inherent in those authors' formalism breaks down, and D is replaced in the near field by $D^{NF} = 2\pi D^2 / \Lambda$, where the
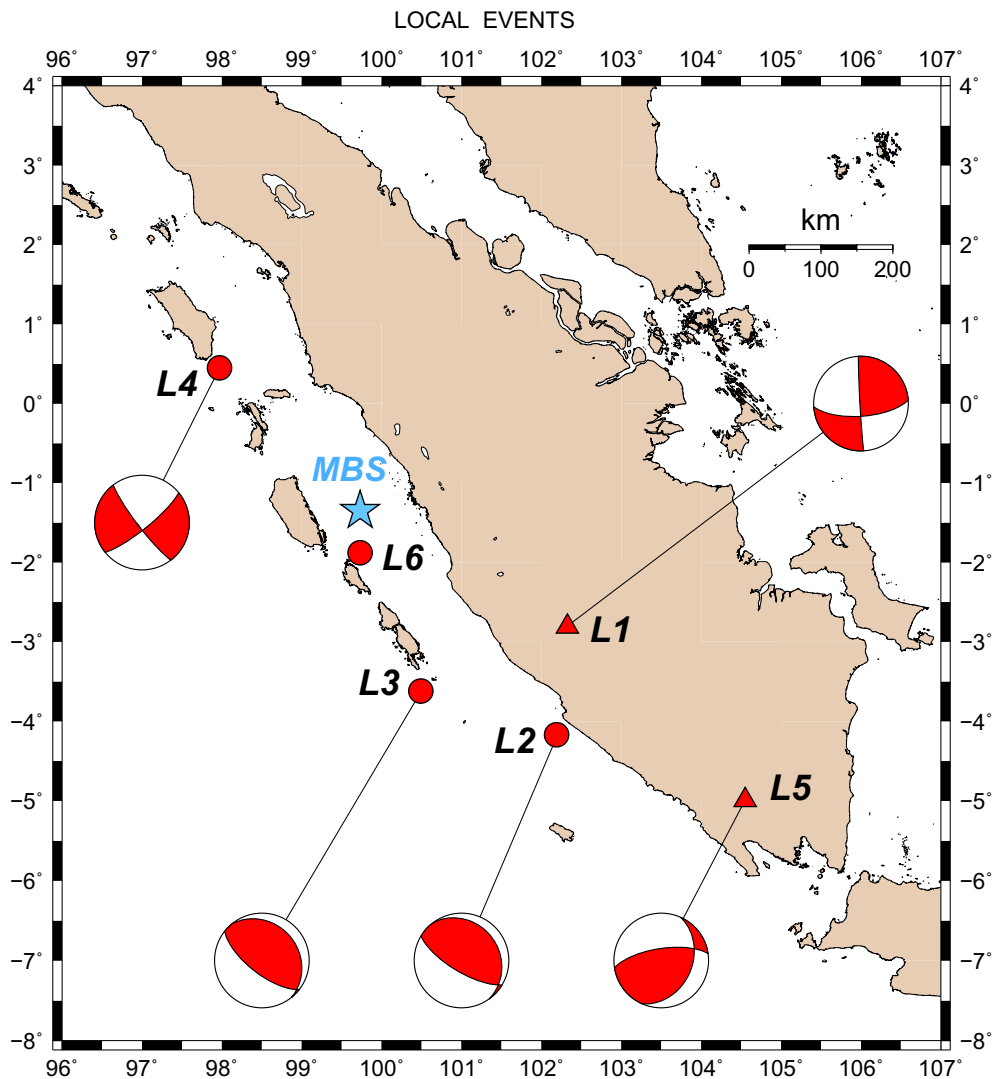
LOCAL EVENTS

Figure 10

Map of the epicenters of local earthquakes detected at regional distances by the pressure sensor at MBS (blue star). Shallow events ($h < 70$ km) are shown as full circles, intermediate ones as triangles. Codes refer to Table 2. Also shown are GlobalCMT solutions, except for Event L6

wavelength $\Lambda = 40$ km is computed at a typical period of 5 s.

Results are listed in Table 2, where E_P^E is scaled to the published M_0, yielding a pressure-estimated energy-to-moment parameter Θ_P. Figure 11 plots E_P^E vs. published moment M_0. It is not possible to compare directly Θ_P to values of Θ computed from seismograms at teleseismic distances, because the regional events detected during our deployment are too small ($M_0 \leq 4.7 \times 10^{24}$ dyn $* $ cm) to lend

themselves to a routine global computation of Θ. Nevertheless, it is remarkable that the range of computed values of Θ_P (-4.57 to -5.47) is typical of values measured at subduction zones (Newman and Okal 1998). In the case of the smallest (and closest) Event L6, for which no seismic moment is available, a tentative value of $M_0 = 2.9 \times 10^{23}$ dyn*cm can be estimated by scaling the moment of Event L3 using the difference of body wave magnitudes (4.5 vs. 4.7), in a range of sizes where m_b has
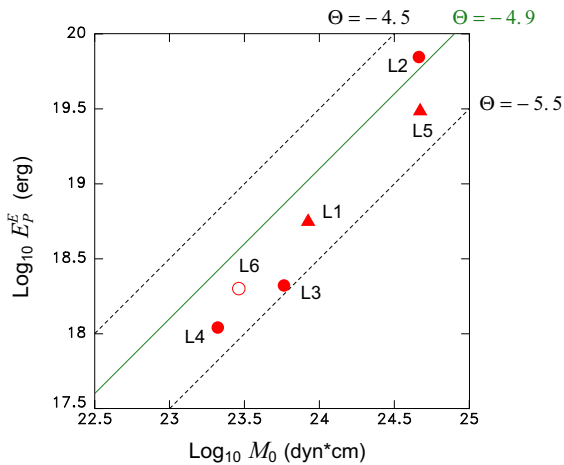
Figure 11

Pressure-estimated seismic energy E_P^E at MBS vs. published seismic moment M_0. Circles refer to shallow events, triangles to intermediate ones. The open circle is for event L6, whose moment is estimated on the basis of its body-wave magnitude m_b. The green line shows the predicted theoretical value, $\Theta = -4.90$ (Newman and Okal 1998)

started to saturate (Geller 1976; Okal 2019), and under the assumption that those events follow scaling laws. This results in a tentative value of $\Theta_P = -5.18$, again in excellent agreement with values expected at subduction zones, and it confirms that an estimated quantification of seismic sources in the near field can be obtained at high frequencies, even at very short distances and for small events.

6. Discussion and Conclusions

During a 48-day window of continuous operations, we were able to detect 16 earthquakes—six at regional distances and ten global events at teleseismic
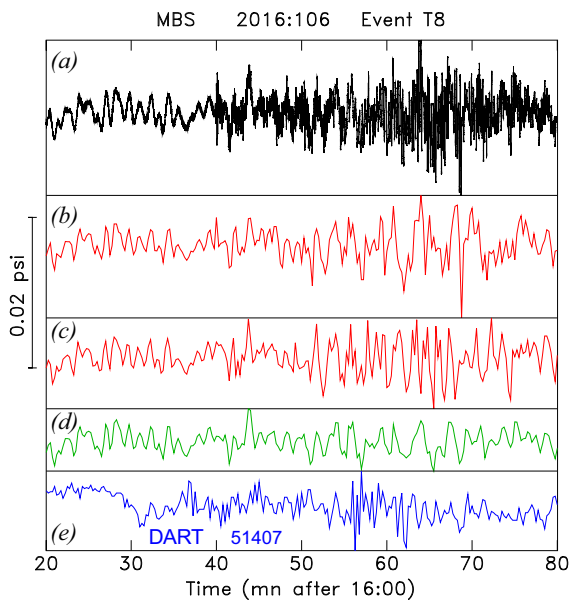

Figure 12

Event T8 (Kyushu) recorded by the pressure sensor at MBS and by the DART station 51407. **a** Original MBS trace. **b** Record decimated by keeping one point every 15 s. **c** Same as (**b**), but offset by 7.5 s. **d** Record decimated using a 15-s moving average. **e** High-density time series (sampled at 15 s) at DART station 51407. See text for details
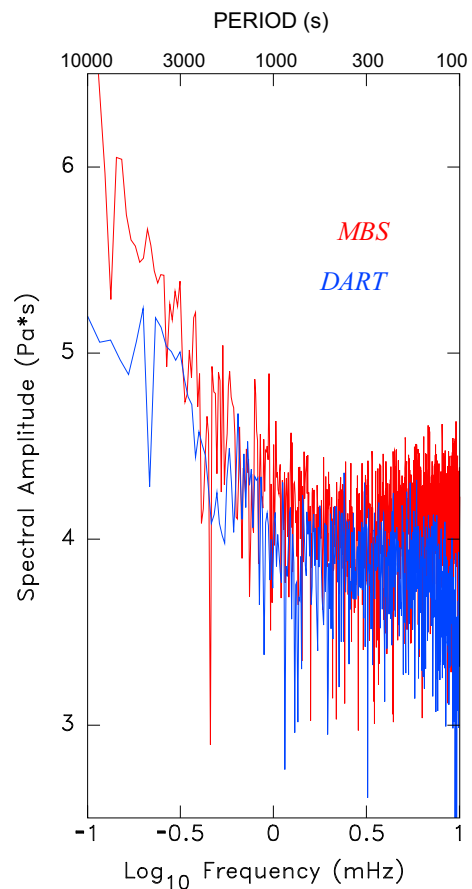

Figure 13

Low-frequency background spectral amplitude for a 24-h seismically quiet time window (18 April 2016) recorded by the sensor at MBS (red) compared with its counterpart at the DART station 51407 (blue). The scales are common to both plots. Note the generally similar amplitudes between 600 and 3000 s

Table 1

Teleseismic events recorded in this study

Code	Date	Origin time	Epicenter		Depth	Global values			Distance	Local estimates			Region
	D M (J) Y	GMT	(°N)	(°E)	(km)	M_0†	M_s	Θ	(°)	M_s	E^{Ea}	Θ	
T1	03 APR (094) 2016	08:23:52	−14.32	166.85	26	22	6.8	−4.89	67.51	6.7	35.9	−4.79	Vanuatu
T2	06 APR (097) 2016	06:58:48	−14.07	166.62	24	13	6.8	−4.90	67.27	6.4	22.5	−4.76	Vanuatu
T3	06 APR (097) 2016	14:45:30	−8.20	107.39	29	1.5	5.4	−4.92	10.2	5.4	2.67	−4.75	Java
T4	07 APR (098) 2016	03:32:54	−13.98	166.59	28	11	6.7	−5.00	67.23	6.5	8.93	−5.09	Vanuatu
T5	10 APR (101) 2016	10:28:59	36.47	71.13	212	11		−4.34	46.15		23.5	−4.67	Hindu Kush (Intermediate)
T6	13 APR (104) 2016	13:55:18	23.10	94.68	136	32		−4.46	24.87		114.	−4.45	Myanmar (Intermediate)
T7	13 APR (104) 2016	18:21:53	7.79	122.02	17	1.1	5.6	−4.96	24.02	5.7	0.82	−5.13	Mindanao, Philippines
T8	15 APR (106) 2016	16:25:06	32.79	130.75	10	45	7.3	−5.00	44.90	7.2	27.2	−5.22	Kyushu
T9	16 APR (107) 2016	23:58:37	0.35	−79.93	21	590	7.5	−5.15	178.95		167.		Ecuador
T10	28 APR (119) 2016	19:33:24	−16.04	167.38	24	36	7.1	−4.71	68.16	6.9		−4.33	Vanuatu

[a] Moment values are in in units of 10^{25} dyn*cm; Estimated Energies in 10^{20} erg

Table 2

Local events recorded in this study

Code	Date	Origin time	Epicenter		Depth	Global values		Distance	Local estimates			Region
	D M (J) Y	GMT	(°N)	(°E)	(km)	M_0†	m_b	(km)	F_P[a]	E_P^{Ea}	Θ_P	
L1	29 MAR (089) 2016	06:24:48	−2.807	102.319	160	8.4	5.1	329.9	24.6	0.56	−5.18	Southern Sumatra (Intermediate)
L2	10 APR (101) 2016	02:14:35	−4.149	102.211	41	26.	6.0	414.9	194.	6.99	−4.81	Southern Sumatra
L3	15 APR (106) 2016	10:24:31	−3.620	100.492	38	5.8	4.7	265.3	12.4	0.21	−5.44	Southern Sumatra
L4	16 APR (107) 2016	21:09:12	0.450	97.971	10	2.1	5.1	279.7	6.84	0.11	−5.28	Northern Sumatra
L5	02 MAY (123) 2016	04:21:25	−4.989	104.551	115	47.	6.0	669.8	32.7	3.06	−5.19	Southern Sumatra (Intermediate)
L6	03 MAY (124) 2016	22:32:36	−1.875	99.734	35	2.9[b]	4.5	58.2	3.30	0.20	*−5.16*[b]	Southern Sumatra

[a] Moment values are in in units of 10^{23} dyn*cm; Fluxes in g/s², Estimated Energies in 10^{19} erg.

[b] For Event L6, values in *italics* are estimated from scaling laws (Geller 1976; Okal 2019)

distances, for which meaningful quantifications of the seismic source were obtained and for all but one small event, successfully compared to globally published values. These results verify the concept of using a seafloor pressure sensor to quantify the source of a seismic event, particularly in the near field.

A remarkable advantage of our instrument is its high sampling rate, made possible by the lone physical variable measured (pressure), as opposed to a more traditional three-component seismometer. In this respect, it also differs fundamentally from DART sensors (Meining et al. 2005), built for the exclusive detection of tsunami waves in a range of frequencies for which their finest sampling (1 point every 15 s; only available in real time in triggered mode) is adequate, but precludes the recording of conventional body and surface seismic waves. We further examine this question on Fig. 12, where we have decimated the MBS record of Event T8, our largest non-antipodal teleseismic event, shown in black on Frame (a), to the DART standard of 15 s. The time series in Frame (b) (in red) was obtained by just retaining one point every 15 s, starting with the first sample in (a), while Frame (d) (in green) represents a moving average of (a), integrated over 15-s wide windows. Frame (c) (also in red) is equivalent to (b) but is offset half a time sample (7.5 s). As expected, we document the essential disappearance of the body wavetrains, and the total aliasing of the standard 20-s Rayleigh waves. Note in particular that their remaining pattern depends on the detail of the decimation strategy, with the sliding window degrading them most efficiently; in addition, subtle variations in the crude decimating algorithm can result in significant differences in waveshape, as shown by Frames (b) and (c). By contrast, the lower-frequency mantle waves are preserved, but their quantitative processing is made impossible by ambient noise. In Fig. 12e, we further compare our results to a high-sampling record of Event T8 at DART station 51407, located off the Big Island of Hawaii (none are available for that date in the Indian Ocean); its waveshape (in blue) is generally comparable to the decimated time series (b) or (c), reflecting the coarse sampling of the DART sensor, as opposed to the sliding average process in (d). At any rate, in this particular instance, the background noise of the DART record similarly

prevented its use to quantify the long-period spectrum of the seismic source.

At even longer periods characteristic of tsunami waves, and on a day (18 April 2016) without major seismic events, we compare on Fig. 13 the background spectral amplitudes at the Mentawai Basin Sensor (MBS) and at the DART station 51407. We find very comparable levels in the range of periods typical of large tsunamis (600–3000 s), while the MBS sensor is found significantly noisier both at shorter periods characteristic of seismic mantle waves (100–300 s), and at periods beyond 1 h, which are generally longer than those of tsunamis. These results suggest that the type of sensor used in this preliminary study could detect a typical tsunami wave with a performance comparable to that of a DART station.

There remains the caveat that, given the short nature of our experiment, neither a truly large earthquake (except the antipodal Ecuadorian event T9), nor a significant local one, were detected at MBS. In particular, none of the 16 events generated any gravitational water wave detectable by our pressure sensor. Only the continuous operation of the sensor over a much longer period of time will allow us to eventually expand our investigation to this condition, in fulfillment of the motivation of our project.

Publisher's Note Springer Nature remains neutral with regard to jurisdictional claims in published maps and institutional affiliations.

REFERENCES

Boatwright, J., & Choy, G. L. (1986). Teleseismic estimates of the energy radiated by shallow earthquakes. *Journal of Geophysical Research*, *91*, 2095–2112.

Borrero, J. C., Sieh, K., Chlieh, M., & Synolakis, C. E. (2006). Tsunami inundation modeling for Western Sumatra. *Proceedings of the National Academy of Sciences B*, *103*, 19673–19677.

Borrero, J. C., Weiss, R., Okal, E. A., Hidayat, R., Arcas, S., & Titov, D. V. V. (2009). The tsunami of 2007 September 12, Bengkulu Province, Sumatra, Indonesia: Post-tsunami survey and numerical modeling. *Geophysical Journal International*, *178*, 180–194.

Cohen, L. (1989). Time-frequency distributions—a review. *Proceedings of the Institute of Electrical and Electronic Engineering*, *77*, 941–981.

Dziewonski, A. M., Chou, T. A., & Woodhouse, J. H. (1981). Determination of earthquake source parameters from waveform data for studies of global and regional seismicity. *Journal of Geophysical Research*, *86*, 2825–2852.

Ebeling, C. W., & Okal, E. A. (2012). An extension of the E/M_0 tsunami earthquake discriminant Θ to regional distances. *Geophysical Journal International*, *190*, 1640–1656.

Ekström, G., Nettles, M., & Dziewoński, A. M. (2012). The global CMT project, 2004–2010: Centroid moment tensors for 13,107 earthquakes. *Physics of the Earth and Planetary Interiors*, *200*, 1–9.

Geller, R. J. (1976). Scaling relations for earthquake source parameters and magnitudes. *Bulletin of the Seismological Society of America*, *66*, 1501–1523.

Haskell, N. A. (1953). The dispersion of surface waves on multilayered media. *Bulletin of the Seismological Society of America*, *43*, 17–34.

Meining, C., Stalin, S., Nakamura, A.I., González, F.I., & Milburn, H.B. (2005). In Technology developments in real-time tsunami measuring, monitoring and forecasting, *Proceedings of the OCEANS 2005 MTS/IEEE Conference,* pp. 1673–1679, Washington, D.C.

Mendiguren, J. (1971). Focal mechanism of a shock in the middle of the Nazca plate. *Journal of Geophysical Research*, *76*, 3861–3879.

Mungov, G., Eblé, M., & Bouchard, R. (2013). DART tsunameter retrospective and real-time data: A reflection on 10 years of processing in support of tsunami research and operations. *Pure and Applied Geophysics*, *170*, 1369–1384.

Natawidjaja, D. H., Sieh, K., Chlieh, M., Galetzka, J., Suwagardi, B. W., Cheng, H., et al. (2006). Source parameters of the great Sumatran megathrust earthquakes of 1797 and 1833 inferred from coral microatolls. *Journal of Geophysical Research*, *B6*, B06403. (37 pp).

Newman, A. V., & Okal, E. A. (1998). Teleseismic estimates of radiated seismic energy: The E/M_0 discriminant for tsunami earthquakes. *Journal of Geophysical Research*, *103*, 26885–26898.

Okal, E. A. (1992). A student's guide to teleseismic body-wave amplitudes. *Seismological Research Letters*, *63*, 169–180.

Okal, E. A. (2019). Energy and magnitude: A historical perspective. *Pure and Applied Geophysics*, *176*, 3815–3849.

Okal, E. A., & Talandier, J. (1989). M_m: A variable period mantle magnitude. *Journal of Geophysical Research*, *94*, 4169–4193.

Paros, J., Migliacio, P., Schaad, T., Meining, C., Spillane, M., Stalin, S., & Chadwick, W. (2012). Nano-resolution technology demonstrates promise for improved local tsunami warnings on the MARS project. In *Proceedings of the OCEANS 2012 IEEE Conference, 12,* 6 pp., Hampton Roads, Virginia.

Saloor, N., & Okal, E. A. (2018). Extension of the energy-to-moment parameter Θ to intermediate and deep earthquakes. *Physics of the Earth and Planetary Interiors*, *274*, 37–48.

Sella, G. F., Dixon, T. H., & Mao, A. (2002). REVEL: A model for Recent plate velocities from space geodesy. *Journal of Geophysical Research*, *107*(B4), ETG-11. (32 pp).

Vaněk, J., Zátopek, A., Kárník, V., Kondorskaya, N. V., Riznichenko, Yu. V., Savarenskiĭ, E. F., et al. (1962). Standardizatsya shkaly magnitud. *Izvestiya Akademii Nauk SSSR, Seria Geofizicheskaya*, *2*, 153–158 (in Russian; English translation, *Bulletin of the USSR Academy of Sciences*, *Geophysics Series*, *2*, 108–111).

Wessel, P., & Smith, W. H. F. (1991). Free software helps map and display data. *Eos, Transactions of the American Geophysical Union*, *72*, 441 and 445–446.

Zachariasen, J., Sieh, K., Taylor, F. W., Edwards, R. L., & Hantoro, W. S. (1999). Submergence and uplift associated with the giant 1833 Sumatran subduction earthquake: Evidence from coral microatolls. *Journal of Geophysical Research*, *104*, 895–919.